Ⓔ

Estimation of Lateral Variations of the Mohorovičić Discontinuity Using 2D Modeling of Receiver Functions

by Rumi Takedatsu and Kim B. Olsen

Abstract   We used 2D finite-difference modeling and azimuthally binned receiver functions (RFs) to explore whether abrupt offsets in Moho depth can be detected by one or a few closely spaced P-wave RFs. Our results show that 2D synthetic RFs generated in the immediate vicinity above a Moho depth change can provide important clues to the abruptness of the offset. In particular, diffraction of the waves impinging onto the Moho offset may generate a split P_S arrival, causing systematic variation of peak-to-peak P-P_S delay times with increasing ray parameter, depending on the location relative to the Moho offset and the incidence direction of the RFs. We outline an approach using a slant-stack method to constrain the location of a relatively abrupt depth change of Moho ($\gtrsim 45°$) using separate RF stacks incident from opposite directions. For a station located on the western border of the Caspian Sea in Azerbaijan (LKR), our 2D models with an ∼8 km transition from a shallower Moho to the east and deeper Moho to the west generate synthetic RFs with features in general agreement with observations. These models, which include step- and ramp-like offsets of Moho, are in general agreement with estimates of crustal thickness from seismic data. Thus, our results suggest that characteristics in one or a few azimuthally binned radial P-wave RFs can be used in concert with a slant-stack analysis to pinpoint a relatively abrupt change in underlying Moho depth.

Online Material: Discussion and figures of a verification study of receiver functions (RFs) computed by different methods, crustal phases generated in our 2D model using animations of the simulated wave propagations, as well as estimated crustal structures, and RFs for Moho offset models, including realistic levels of noise.

Introduction

The boundary between the crust and upper mantle, often referred to as the Mohorovičić discontinuity or Moho, marks a significant change in seismic velocity and other physical parameters. Conventionally, receiver function (RF) techniques from all available azimuths have been used to estimate crustal thickness assuming a locally horizontal Moho discontinuity, employing a 1D method to propagate the waves (e.g., f-k methods, Fuchs and Müller, 1971). When RFs from a linear array of closely spaced stations are available, migration techniques can be used to obtain an enhanced image of the details of the Moho topography, in the vicinity of faults, interface topography, and other strong lateral variation in the crust (e.g., Kosarev *et al.*, 1999; Bostock *et al.*, 2002).

Often, however, only data from a single station or from stations spaced too far apart to allow for migration near such suspected discontinuity is available. This may be the case if only one station produces a clean signal, if stations are too

widely separated to migrate the data, when inferring Moho depth from sparse arrays designed for earthquake detection, and for stations on the edge of a body of water that prevent imaging except from one side. In such situations, use of 2D/3D modeling of the RFs may be the only possibility to resolve diffractions generated at abrupt details of the Moho geometry (e.g., Yan and Clayton, 2007). Here, we use a 2D finite-difference (FD) algorithm combined with the slant-stacking technique by Zhu and Kanamori (2000; hereafter referred to as ZK2000) with azimuthally binned data to pinpoint the range of a possible Moho offset below single-station RF records.

The article is organized as follows. First, we describe the incentive to our study by the RF data and geological setting from Azerbaijan, where strong lateral variation in the Moho is expected from other geological studies. Next, we present synthetic seismograms for an incident planar P wave traveling through simple crustal models containing various

(a)

(b)
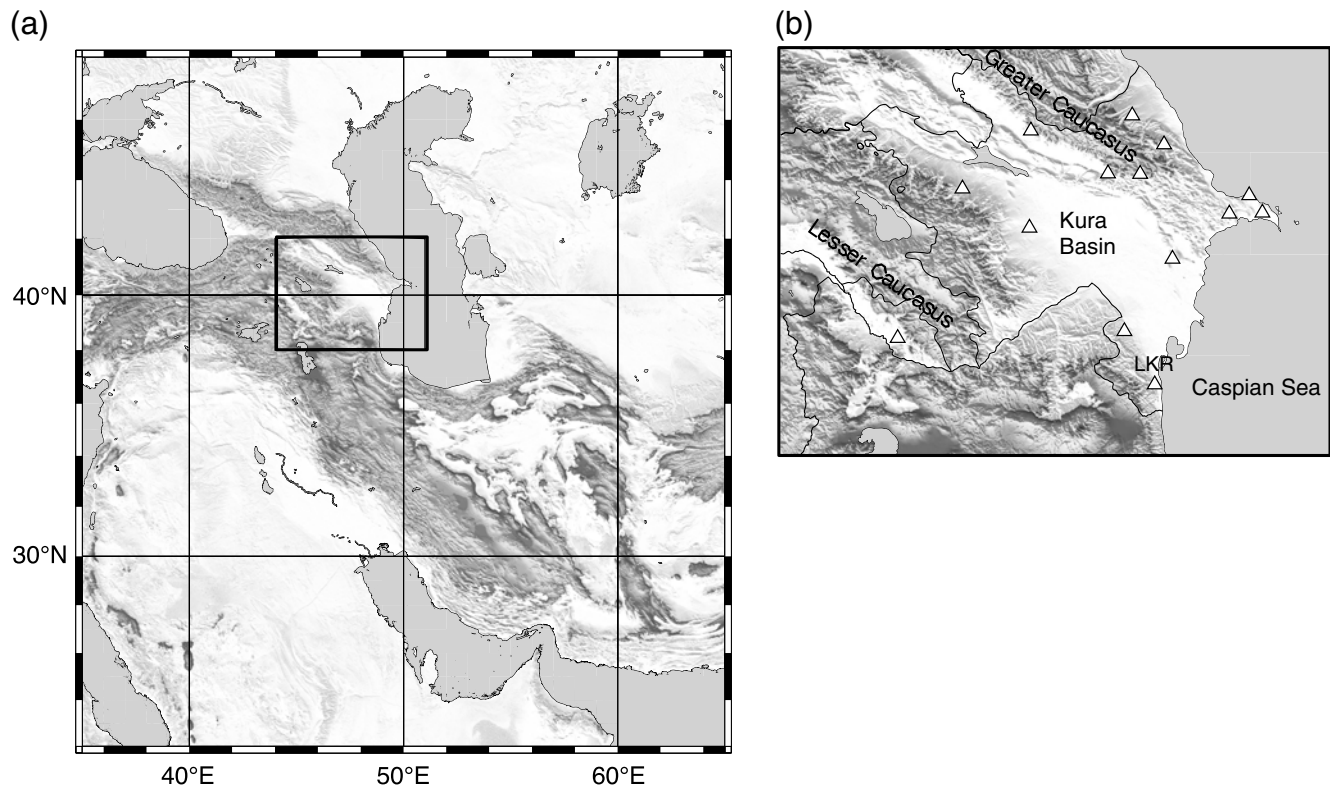
Figure 1. (a) The large continental collision zone between the Eurasian and Arabian plates. The rectangle shows the location of Azerbaijan. (b) Azerbaijan, with the location of 14 stations, including LKR station, depicted.

degrees of lateral change in Moho depth, calculated using a 2D FD algorithm. The synthetic seismograms are used to calculate RFs mainly by the iterative deconvolution method (Ligorria and Ammon, 1999). We examine whether the slant-stacking technique, which is based on 1D wave propagation, can be used to accurately estimate a relatively abrupt Moho depth variation from the synthetic RFs. Finally, the theoretical background from estimating lateral variation of the Moho using 2D RF modeling established in the synthetic RFs study is applied to the observed data from Azerbaijan.

A Case for Single-Station RF Analysis

Azerbaijan, including the Caucasus Mountains and the Caspian Sea, is located on the northern edge of the Eurasian–Arabian plate corrosion zone, a part of the Alpine–Himalayan belt (Fig. 1a), where a long tectonic history has created a complex crustal structure. There is prominent topography in Azerbaijan, such as the Greater Caucasus at the northern boundary and the Lesser Caucasus creating the southwestern boundary in terms of tall mountains, the Kura basin in between these mountains in terms of low topography, and the Caspian Sea to the east (Fig. 1b). In particular, the South Caspian basin is one of the deepest basins (20–25 km) in the world and filled by very thick (~20 km) sediments with a crustal thickness of 35–40 km, and the exact origin and age are not well understood (Mangino and

Priestly, 1998; Brunet et al., 2003; Knapp et al., 2004). One possibility is that the South Caspian basin was opened at the onset of oceanic spreading or as a back-arc basin (Brunet et al., 2003). Other studies suggest that the basin is a remnant of oceanic crust (Kadinsky-Cade et al., 1981) or that the basin was opened on a major Cretaceous strike-slip zone along the Kopet Dag–Alborz–Greater Caucasus mountain belts, making it a large-scale pull-apart continental crustal basin (Sengör, 1990).

According to Gök et al. (2011), the Kura basin has relatively slow S-wave velocity (~2.7–2.9 km/s) in the upper crust (0–11 km), increasing to ~3.8–3.9 km/s in the lower crust based on analyses of a 3D velocity model developed from joint inversion of RFs and surface-wave dispersion. The study also shows that the depth to Moho generally increases from south to north and changes from shallower depths in the Arabian plate (~35 km) to deeper depths at the southern edge of the Greater Caucasus (~54 km). The Kura basin and the western edge of the Caspian Sea show variation of Moho depths between 35 and 45 km (Gök et al., 2011).

The Data Set

Seismic data are available from 14 broadband seismic stations in Azerbaijan from 2003 to 2009 (Fig. 1b), recorded by three-component STS-2 seismometers, with approximately constant sensitivity to frequencies between 0.02 and 50 Hz. Seismic events with distances between 30° and 95° (in
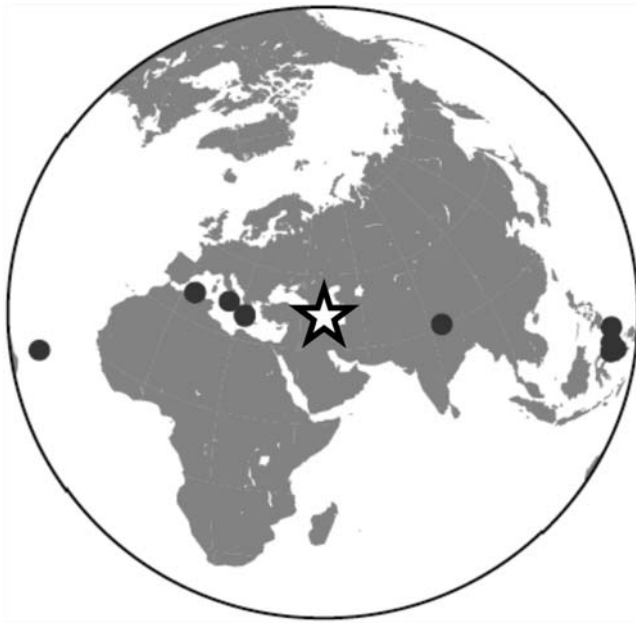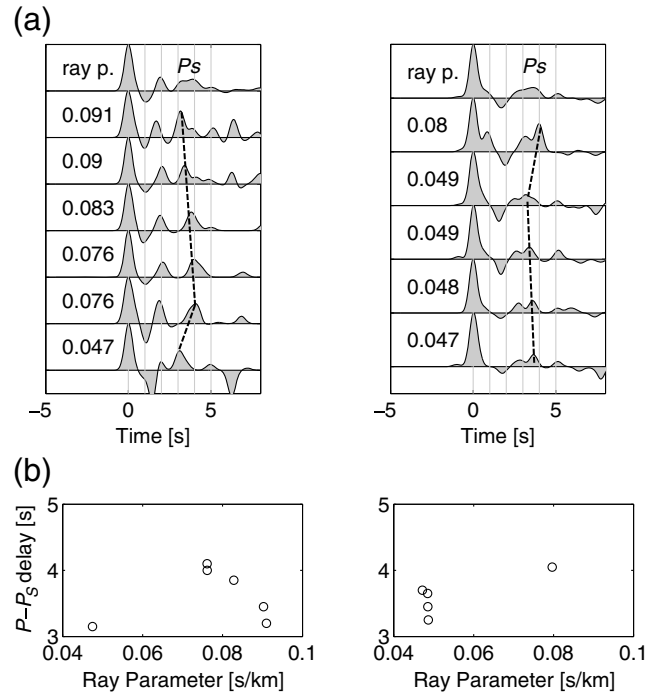
Figure 2. The location of Azerbaijan (star) and selected events from the east and west (dots) used in this study.


Figure 3. (a) Receiver functions (RFs) at station LKR as a function of ray parameters (ray p.) for sources incident from (left) the west and (right) the east. Peak P_S arrivals are outlined by dashed lines. The numbers on the left of the RFs list the ray parameters. The uppermost RFs are generated from a stack of all RFs shown below. (b) P-P_S delay times for sources incident from (left) the west and (right) the east.

which the P_S conversion is best developed) and magnitude equal to or larger than 5.5 were selected. These selected events were used to generate observed radial RFs using the iterative time-domain deconvolution method (Ligorria and Ammon, 1999) with Gaussian widths of 3.0 Hz. Only LKR was found suitable for further analysis, because of its location and a deficient signal-to-noise ratio (SNR) from the remaining stations.

LKR is located on the southern boundary of the Kura basin (see Fig. 1b). Gök *et al.* (2011) find that the tangential RFs at LKR contain significant amounts of energy, suggesting lateral variation around the station. We use the RFs for eastern back azimuths (five events, here defined as 90°–100°) and western back azimuths (six events, here defined as 260°–290°) (Fig. 2), incident approximately perpendicular to the proposed north–south-trending Moho offset implied by Gök *et al.* (2011). The radial RFs are sorted by ray parameters in Figure 3. Note the multiple arrivals following the P wave, with the larger separation of these arrivals for the events from the west (1–2 s) as compared to the events from the east (<1 s). However, the limited range of ray parameters at the station does not support any systematic trends in P-P_S delay times.

We apply these RFs to estimate crustal thickness, P-wave velocities (V_P), and the ratio between P- and S-wave velocities (V_P/V_S) from the ZK2000 method (assuming V_S is constant), separately for events from the east, from the west, and from both east and west (Fig. 4). From the events from the west, the estimated crustal thickness is 34.7 km, V_P/V_S is 1.74, and V_P is 6.37 km/s. The estimated thickness, V_P/V_S, and V_P are 26.7 km, 1.72, and 6.28 km/s, respectively, for the events from the east and 32.2 km, 1.70,

and 6.23 km/s, respectively, for events from both the east and west. The standard deviation for the crustal thickness along the best V_P/V_S ratio (σ) is estimated using the following procedure: We estimate the crustal thickness and V_P/V_S ratio, seeking the maximum amplitude grid point that is the result of summation of amplitudes for P_S and multiples P_PP_S and $P_PS_S + P_SP_S$ from RFs at various crustal thicknesses and V_P/V_S ratios. The standard deviation (σ) of the crustal thickness is estimated from the residuals between the maximum amplitude and all the other amplitudes along the best V_P/V_S ratio. The standard deviations are shown in Figure 4 by the white lines. When the slant-stack method provides a well-defined solution (e.g., a band of maximum values, shown as the black area in Fig. 4), the estimated crustal parameters are well constrained. In the following, we present the results of a theoretical study based on these characteristics of the observed RFs at LKR to examine whether the ~8 km difference in Moho depth for RFs from opposite directions is an indication of the underlying lateral variation of Moho based on the single-station data.

Numerical Modeling

We use a 2D FD wave propagation method to examine the potential for detecting abrupt topography of the Moho interface. The FD method solves the 2D *P-SV* wave equation
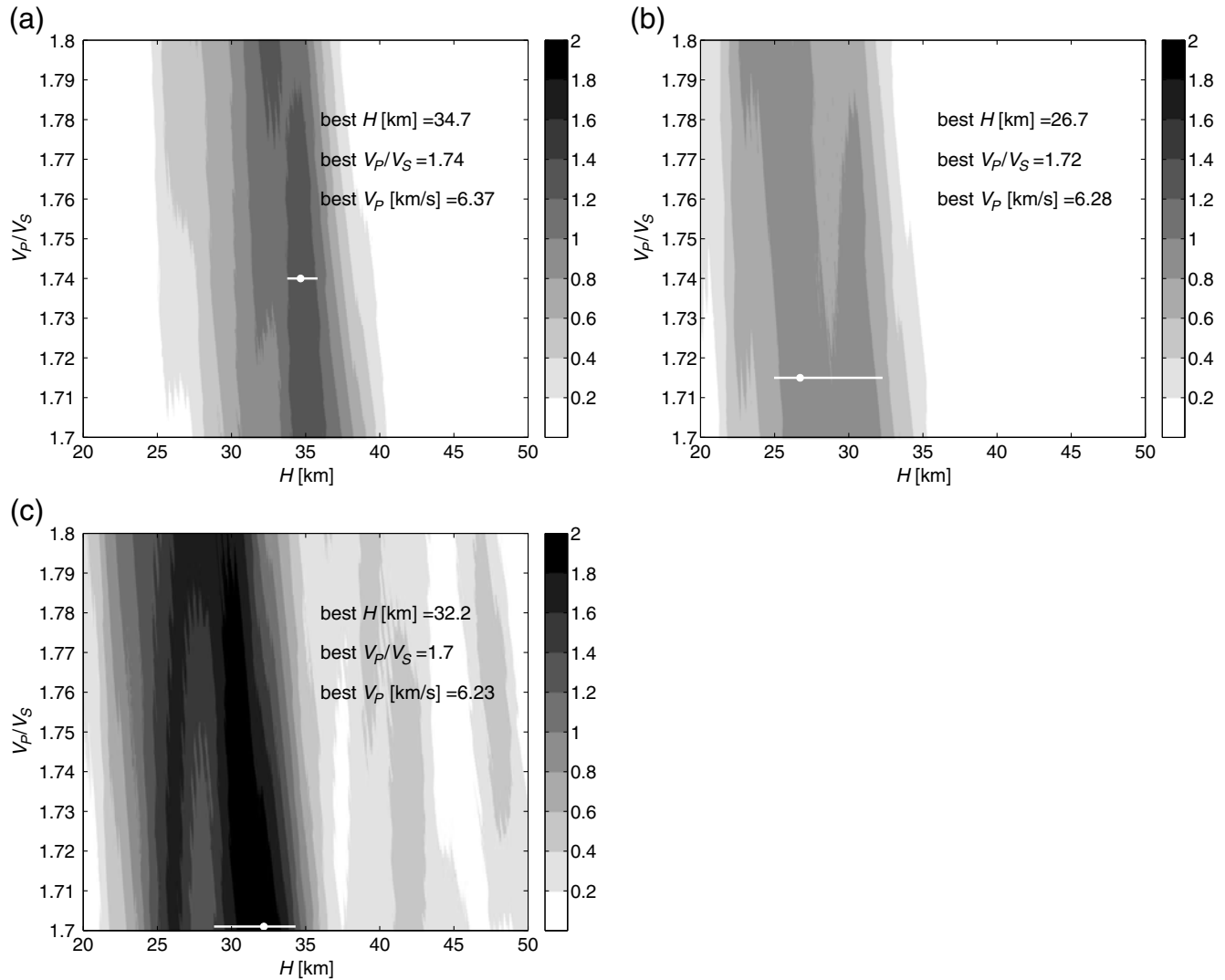
Figure 4. Estimates of Moho thickness and V_P/V_S ratio for (a) events from the west, (b) events from the east, and (c) all events at LKR station using the Zhu and Kanamori (2000; referred as ZK2000) method (white dots), as well as crustal thickness (H) $\pm 1\sigma$ in white lines along the best V_P/V_S ratio. V_S is considered constant, equal to 3.66 km/s for the crust and 4.25 km/s for the upper mantle (Gök *et al.*, 2011), and we obtain V_P from the estimated V_P/V_S ratios. The gray scale shows weighted, normalized (0–2) stacked amplitudes from P_S, $P_P P_S$, and $P_P S_S + P_S P_S$ arrivals at each grid point extracted from the RFs.

in the form of partial differential equations on a staggered grid and is fourth-order accurate in space and second-order accurate in time (Levander, 1988). Absorbing boundary conditions are used at the sides and bottom (Cerjan *et al.*, 1985), and a flat free-surface boundary condition is at the top (Gott-schaemmer and Olsen, 2001).

Plane-Wave Source Description

We generate plane-wave source functions as point sources evolving in unison at the nearest grid points defining a line of the desired inclination. The source time history is taken as the positive amplitudes of a cosine function with a width of 0.4 s and containing frequencies up to 5 Hz. We use a Gaussian filter with a nominal cutoff frequency of 3 Hz for our RF calculations, which essentially removes signals with

frequencies above ~2.4 Hz. This bandwidth ensures at least five points per minimum (shear) wavelength in our model, a commonly used rule of thumb for sufficient accuracy for fourth-order FD methods (e.g., Levander, 1988).

Crustal Model

Our 2D finite-difference model has dimensions of 1200 km (along the radial direction) and 1080 km (along the vertical direction), with a grid spacing of 0.3 km everywhere in the model. The relatively large dimensions are used to ensure that the synthetic RFs obtained from the plane-wave source functions are free of artifacts from reflections generated at the grid truncations (due to imperfectly absorbing boundary conditions). We record synthetic seismograms at
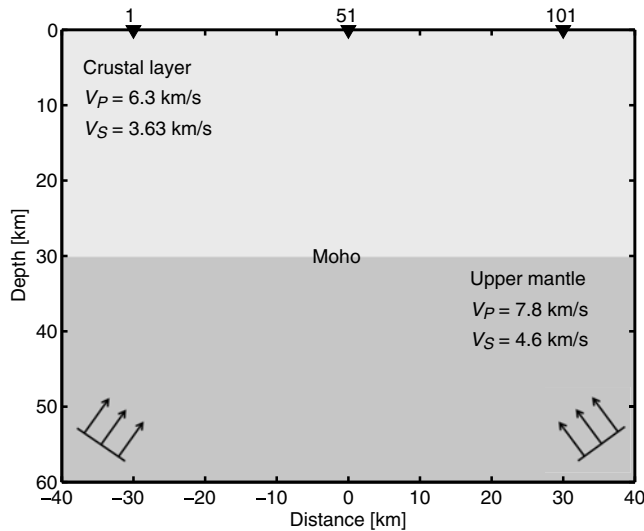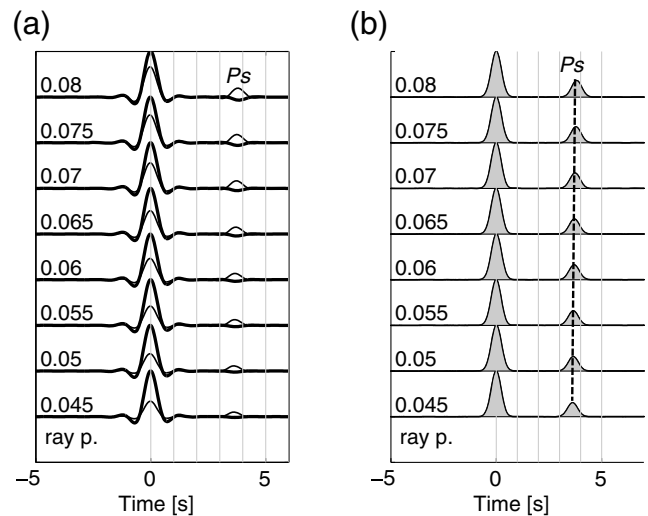
Figure 5. Reference layer-over-half-space model with a flat Moho. Distance 0 km is defined at the center of the model along the radial direction; 101 receivers are located on the surface between −30 and +30 km. The three triangles depict locations of receivers at −30, 0, and +30 km, as stations 1, 51, and 101, respectively. Arrows show the directions of the incident planar *P* waves.

Figure 6. (a) Synthetic seismograms at station 51 calculated in the reference model. The vertical components are shown in thick black lines, and the radial components are shown in thin gray lines. (b) RFs estimated from the synthetic seismograms. The ray parameters are listed at the left of their waveforms. Peak P_S arrivals are outlined by the dashed line. The numbers on the left of the seismograms and RFs list the ray parameters.

101 stations located on the free surface with a separation of 0.6 km.

Reference Model

Figure 5 shows our reference crustal model, a layer over half-space with a horizontal Moho interface located at 30 km depth. V_P for the crust and upper mantle are 6.3 and 7.8 km/s, respectively; V_S are 3.63 and 4.6 km/s, respectively; and densities (ρ) are 2600 and 3300 kg/m^3, respectively (adapted from the parameters of Yan and Clayton, 2007). Plane *P*-wave sources with ray parameters (p) between 0.045 and 0.080 s/km (corresponding to incidence angles between 20.55° and 38.61°, respectively) at an interval of $\Delta p = 0.005$ s/km are then inserted into the upper mantle in the model.

Figure 6a shows vertical and radial components of synthetic seismograms calculated from the reference model, and Figure 6b shows the RFs estimated from the seismograms at station 51. We use an iterative time-domain deconvolution technique (Ligorria and Ammon, 1999) to calculate the RFs. Both the seismograms and RFs are arranged such that the time corresponding to the peak of the *P* wave is at $t = 0$ s, and all amplitudes are normalized by the amplitude of the *P*-wave peak for each RF and smoothed by the 3 Hz Gaussian filter. Moho-converted *P*-to-*S* converted (P_S) waves clearly appear in the RFs, and the arrival-time difference between the *P* and P_S waves increases slightly with increasing ray parameter due to the increasing travel times of the phases in the crust. Ⓔ The accuracy of RFs and P_S/P ratios calculated from the 2D FD model are verified in Figures S1 and S2 in the electronic supplement to this article; animation of the wave propagation for the reference model

and the associated RFs are also shown in Animation S1 and Figure S3, respectively.

In Figure 7, we estimate the crustal thickness (H) with uncertainty (σ) and V_P/V_S ratio using the ZK2000 method for RFs computed from planar *P*-waves incident from both sides. The preferred estimates obtained by the method accurately reproduce the crustal thickness of 30.00 km (estimated 30.16 km), V_P/V_S of 1.740 (estimated 1.739), and V_P of 6.30 km/s (estimated 6.31 km/s).

Moho Offset Model

We now modify the reference model discussed in the previous section by including a Moho step discontinuity located at 0 km, with negative distances on the deep side and positive distances on the shallow side. The depth of the Moho changes from 30 to 38 km at 0 km distance (see Fig. 8, again adapted from Yan and Clayton, 2007).

We use the ZK2000 slant-stack method to test whether we can detect the step-like offset on the Moho from the RFs based on our model. Here, we limit the range of crustal thicknesses and V_P/V_S ratios to 20–50 km and 1.7–1.8, respectively. The Moho depth is estimated from three different source scenario stacks, namely for *P* waves incident from (1) both sides, (2) only the deep Moho side, and (3) only the shallow Moho side onto the step model. The estimated Moho depths are plotted on top of the true step model. All three source scenario RF stacks show abrupt changes of the estimated Moho, but the location of the estimated offset varies. We also test the effects of using fixed V_S or V_P (i.e., the fixed velocity is not optimized, and the other is computed from the best V_P/V_S ratio) for the slant-stacking
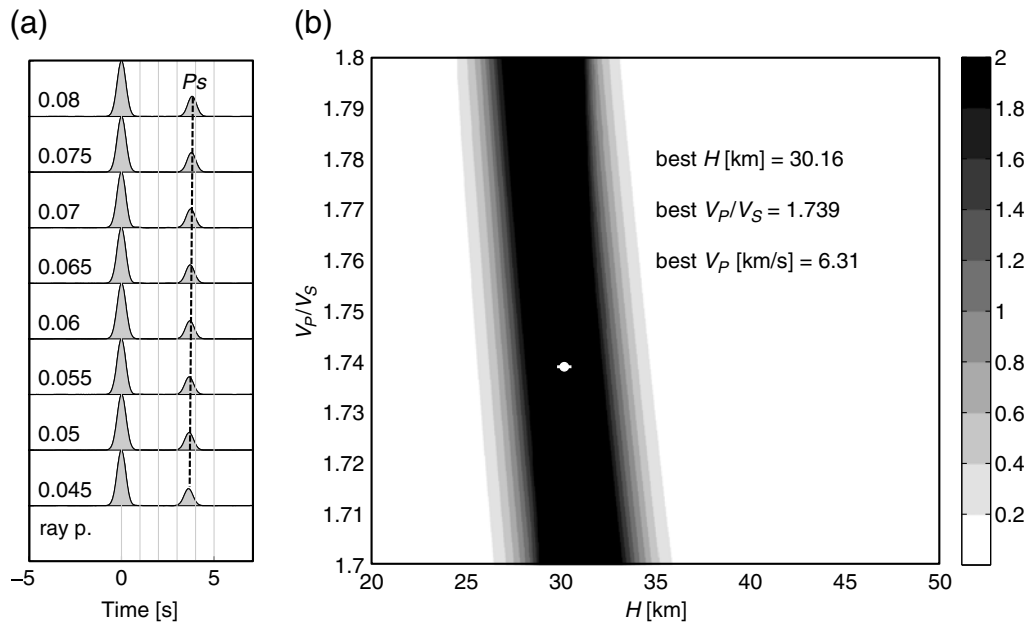
Figure 7. RFs and estimation of Moho depth and V_P/V_S from the ZK2000 method. (a) RFs estimated from the synthetic seismograms in the reference (flat Moho) model, traveling from the left side. Peak P_S arrivals are outlined by the dashed line. The numbers on the left of the RFs list the ray parameters. (b) Result of applying the ZK2000 method to the 16 RFs from both sides. The preferred estimate of Moho depth (H), V_P/V_S ratio, and V_P from the method are listed in the figure. Uncertainty ($\pm 1\sigma$) for the Moho depth is depicted by the white line. See Figure 4 for the explanation of the gray scale.
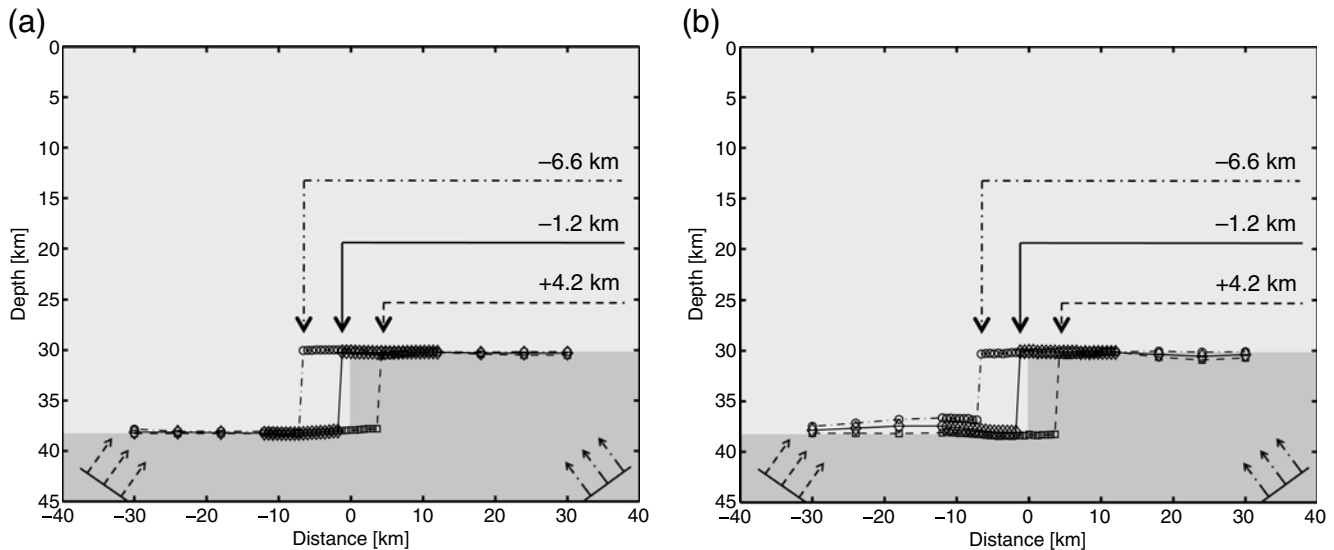

Figure 8. Step model and estimated Moho depth from the ZK2000 method, using (a) fixed V_S and (b) fixed V_P. There are three source scenarios: diamonds with solid lines, source incident from both sides; squares with dashed lines, source incident from the deep Moho side; and circles with long dashed-dotted lines, source incident from the shallow Moho side. The estimated abrupt changes of Moho for the three source scenarios are located at distances −6.6, −1.2, and +4.2 km.

technique (i.e., Fig. 8a,b, respectively). The results using fixed V_S provide a better estimate for the step Moho model, and the best agreement with the true model is obtained for the stack of sources from both sides using fixed V_S, in which the estimated offset is shifted to −1.2 km. The scenario with sources incident from the deep Moho side also shows a good agreement with the true Moho depth change, but the location of the estimated step is shifted to +4.2 km. The scenario with sources incident from the shallower Moho side shows the estimated offset shifted to −6.6 km, due to the different areas of Moho involved in generating the RFs.

The resulting synthetic RFs with various ray parameters at distances −6.6, −1.2, and +4.2 km are shown in Figure 9 for P waves incident from the deep or shallow Moho side.
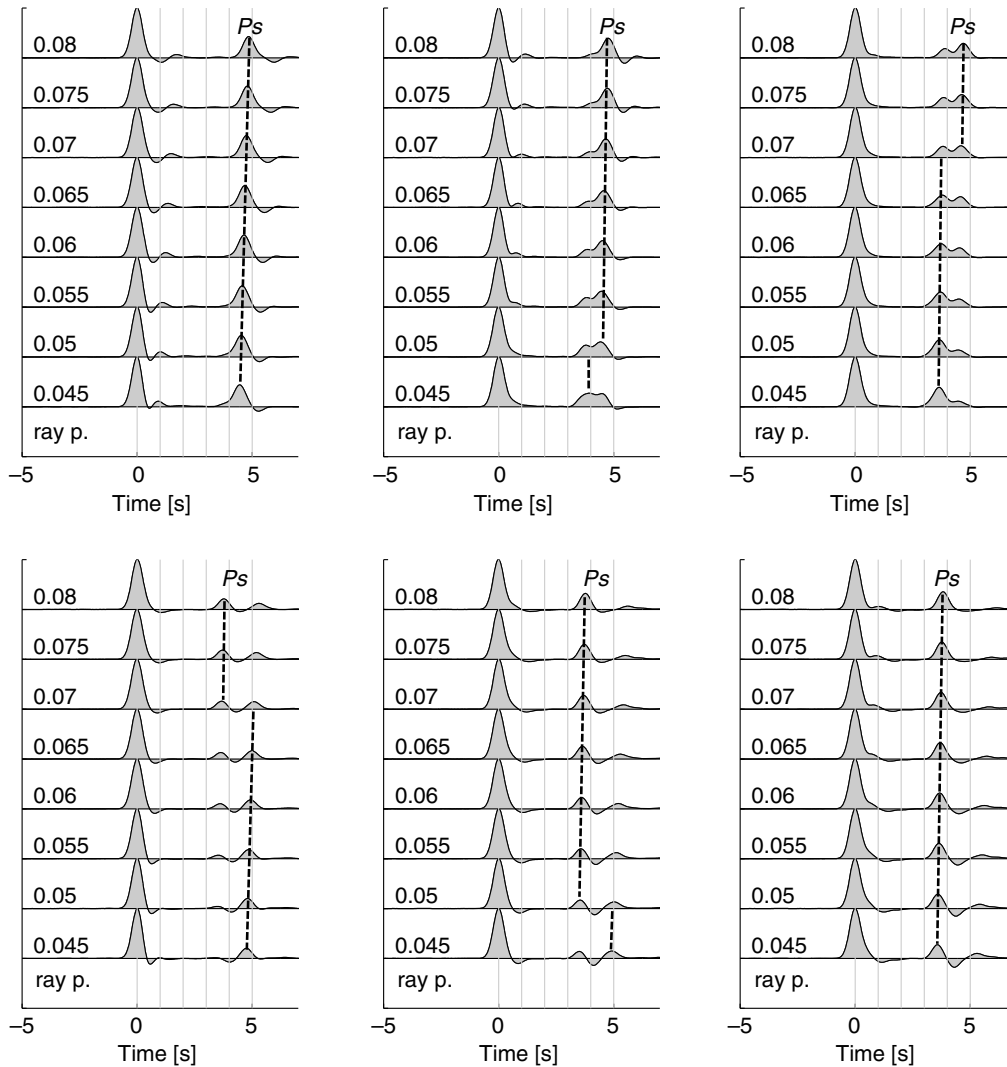
Figure 9.　RFs for the Moho step model in Figure 8a (step model). The top row shows RFs at stations (left) −6.6, (center) −1.2 , and (right) +4.2 km, with seismic waves traveling from the deep Moho side. The bottom row shows RFs at stations (left) −6.6 km, (center) −1.2 km, and (right) +4.2 km, with seismic waves traveling from the shallow Moho side. Peak P_S arrivals are outlined by dashed lines. The numbers on the left of the RFs list the ray parameters.

Notice the P_S waves are divided into two phases to varying degrees, most prominently at distances −6.6 and −1.2 km for sources from the shallow Moho side but also at distances −1.2 and +4.2 km for sources from the deep Moho side, due to interference at the Moho step. The RFs at stations on the shallow Moho side (e.g., distance +4.2 km), for sources from the shallow Moho side, have superimposed P_S phases with smaller ray parameters (steep incidence), and those superimposed P_S phases merge into single P_S phases for larger ray parameters (more oblique incidence). The RFs at distance −6.6 km for sources from the deep Moho side resemble the simplicity of that of a flat Moho model (Fig. 7a). ⒺThe wave interference near the Moho offset is clear in the animation of the wave propagation (Animation S2) and the resulting RFs in Figure S4.

From the RFs, we estimate peak-to-peak arrival-time differences between the P and P_S waves in Figure 9. This

delay between P and P_S for the RFs increases abruptly with increasing ray parameter for sources from the deep Moho side at stations on the shallow Moho side (e.g., for p ∼0.07 at +4.2 km) due to the relative changes in amplitude of the two parts of the split P_S arrival. For the same reason, the P-P_S delay time for the RFs decreases abruptly with increasing ray parameter for sources from the shallow Moho side at stations on the deep Moho side (e.g., for p ∼0.07 at −6.6 km). The RFs from the deep Moho side at distances of −1.2 and −6.6 km show the largest P-P_S arrival-time differences (4–5 s), as compared to the other cases, due to a longer path of the P and P_S waves through the thicker crust.

To assess the accuracy of estimating the Moho offset described above, we repeat the analysis after addition of realistic levels of noise to the RFs. To obtain the noise, we calculate a full stack of the RFs from the 11 observed events recorded at station LKR in Azerbaijan, as well as another
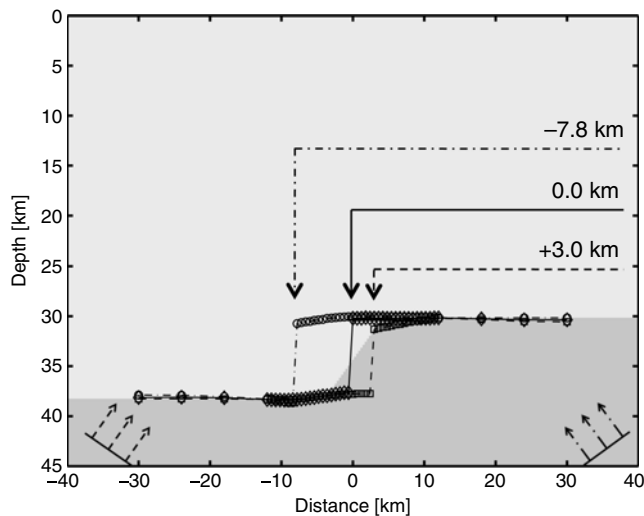
Figure 10. Ramp model and estimated Moho depth from the ZK2000 method for a Moho ramp between −3.9 and +3.9 km. The locations of stations −7.8, 0.0, and +3.0 km depict the horizontal locations of the abrupt change in Moho for the three source scenarios (from the deep side, the shallow side, and both sides). See Figure 8 for the notation of the lines and points.

four partial stacks, using 6 out of the 11 events. The difference between the full and partial stacks is used as an approximation of the noise and is added onto each of the synthetic RFs, following the procedure outlined by Jacobsen and Svenningsen (2008). ⓔ The estimated crustal structures from the three scenarios using RFs with added noise are shown in Figure S5. The best agreement with the true model is again obtained for the stack of sources from both sides, where the estimated offset is located between −0.6 and −1.8 km. The estimated step for the scenario with sources incident from the deep Moho side is located between +3.6 and +5.4 km, showing an abrupt change in crustal thickness from 30 to ∼38 km toward the deep Moho side. The scenario with sources incident from the shallow Moho side shows the estimated offset shifted between −6.0 and −7.2 km. The estimated offsets are generally more distant from the actual offset as compared to those from RFs without noise, but they nevertheless provide a reasonable range. ⓔ The RFs at distances of −6.6, −1.2, and +4.8 km are shown in Figure S6.

Model with a Gradual Change of Moho Depth

For comparison with the abrupt Moho offset model, we produce a new model with a more gradual (ramp-like) change of Moho between −3.9 km (38 km thick crust) and +3.9 km (30-km-thick crust; see Fig. 10). Interestingly, the estimated Moho depths from the ZK2000 method using RFs from the three source scenarios (from deep side, shallow side, and both sides) do not reproduce the ∼45° dip on the Moho, but instead show rather abrupt changes of the interface. For the source incident from both sides, the estimated (abrupt) change in Moho depth is located at 0.0 km on the center of the ramp. The scenario with the source incident

from the shallow Moho side produces an abrupt step on the Moho but shifted to about −7.8 km. The RFs for the wave incident from the deep Moho side outline an abrupt Moho offset up to +3.0 km toward the shallow Moho side from the center of the ramp. RFs for the Moho ramp model at distances −7.8, 0.0, and +3.0 km are shown in Figure 11. The most pronounced effects of the ramp on the RFs include splitting of the P_S arrival at distances of −7.8 km from the shallow side, with an ∼1 s change in peak-to-peak P-P_S delay time at $p = 0.065$–0.070 s/km.

The range of estimated ramp-like change in crustal structures from the three scenarios using RFs with the same four realizations of noise as for the step model discussed above are shown in ⓔ Figure S7. For the source incident from both sides, the estimated abrupt change in Moho depth is located at a distance between the center of the ramp and −0.6 km. The scenario with the source incident from the deep Moho side estimates an abrupt step on the Moho at distances between +1.8 and +4.2 km. The RFs for the source incident from the shallow Moho side outline an abrupt offset shifted between −6.0 and −10.2 km. Thus, the slant-stacking method still produces a reasonable estimate of the Moho offset in the presence of realistic levels of noise in the RFs. ⓔ Figure S8 shows RFs at distances −7.8, 0.0, and +3.0 km.

Method for Estimating the Location of the Moho Offset

For a single-station RF, our results can be compiled into an approach for estimating the approximate position of a potential Moho offset using the ZK2000 slant-stack method with azimuthally binned RFs. If Moho depths estimated from two opposite directions are similar, then a Moho offset is not detected. If Moho depths estimated from the two opposite directions are significantly different (e.g., several kilometers), an offset may be present within a range of possible offset locations dependent on Moho depth, offset, and whether the Moho depth estimated from all RFs is similar to that for the RFs averaged from the shallow Moho side (case 1) or the deep Moho side (case 2). For example, in the case of the 45° ramp at 30–38 km depth in Figure 10, the midpoint of the ramp is located 0–3 km toward the deep Moho side for case 1 and between 0 and 7.8 km toward the shallow Moho side for case 2 (taking averages across grid steps of 0.6 km). In the next section, we will apply this method to LKR.

Discussion

The secondary phases in the events recorded at LKR (Fig. 3) show some similarity to the split P_S phases from our 2D Moho offset models in Figures 9 and 11, although more detailed trends of the shape of the P_S phase with ray parameter are not supported by the data quality. Moreover, the reasonable values and limited variation in the estimated V_P and V_P/V_S ratios for the different azimuthally binned RF
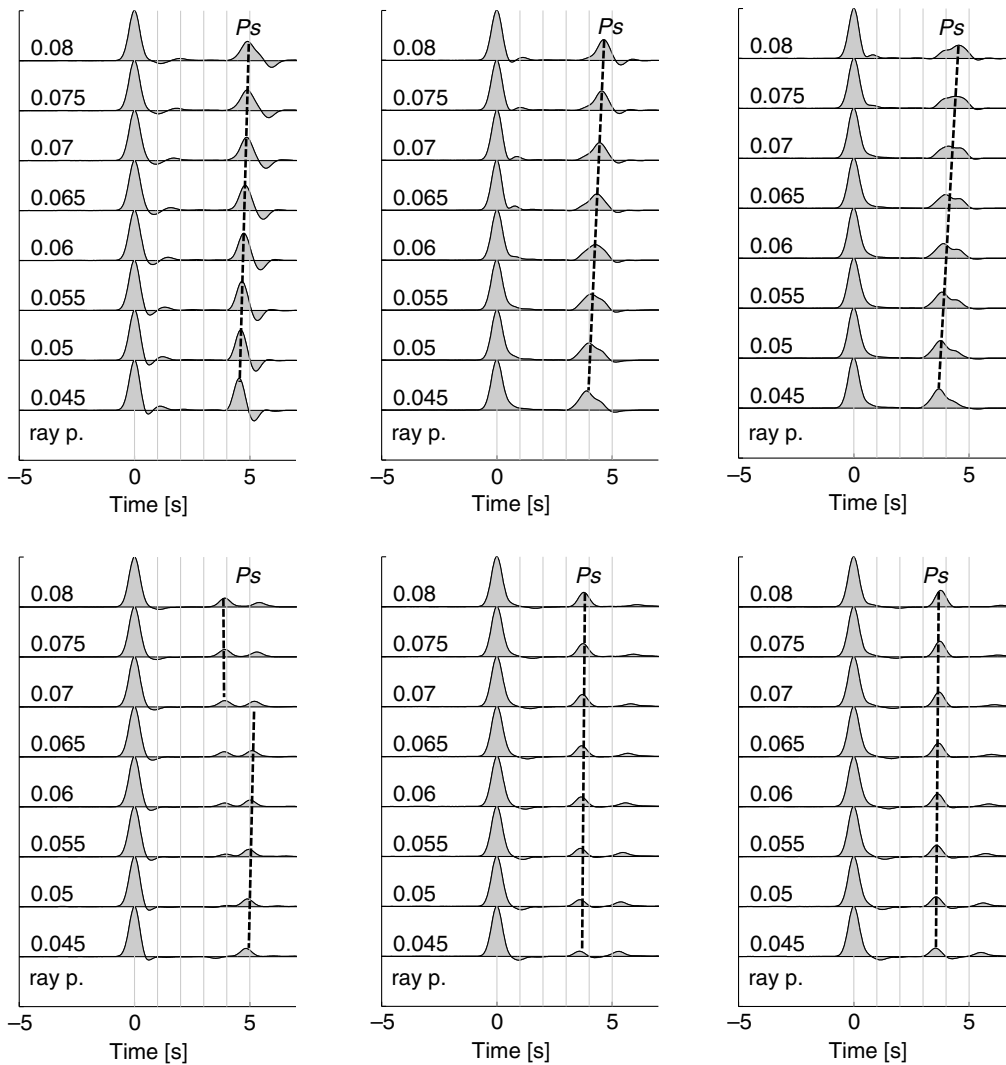
Figure 11. RFs for the Moho ramp model. The top row shows RFs at stations (left) −7.8, (center) 0.0, and (right) +3.0 km, with seismic waves traveling from the deep Moho side. The bottom row shows RFs at stations (left) −7.8, (center) 0.0, and (right) +3.0 km, with seismic waves traveling from the shallow Moho side. Peak P_S arrivals are outlined by dashed lines. The numbers on the left of the RFs list the ray parameters.

stacks provide some confidence in the estimated ∼8 km difference in Moho depth from shallower east to deeper west (see Fig. 4). P-P_S delay times are expected to be in the range of 3.0–4.0 s for Moho depths of 27–35 km and the assumed crustal velocities. For this reason, we expect that the earlier-arriving secondary phase on the RFs (P-P_S delay of ∼2 s; see Fig. 3a,b) for the events from the west may be due to factors other than Moho topography (e.g., intracrustal reflections). The estimated thickness for all events is in between the thicknesses obtained for the events from the east and events from the west (Fig. 4). The elevation of LKR is only 70 m, so we assume the estimated crustal thickness is equal to the estimated Moho depth.

    To apply our results to the Moho topography below LKR, we generated synthetic RFs for step and 45° ramp models of the Moho below the station with parameters specific to

the area and RF sources. Average velocities in the crust and the upper mantle are estimated from Gök *et al.* (2011): V_P of 6.34 km/s and V_S of 3.66 km/s in the crust and V_P of 7.61 km/s and V_S of 4.25 km/s in the upper mantle. Plane P-wave sources with ray parameters between 0.047 and 0.08 s/km for the east events and 0.047 and 0.091 s/km for the west events are inserted. Figure 12 shows the estimated crustal thicknesses from the ZK2000 method. The estimated abrupt change from the step model is located within an interval between −7.2 and −2.4 km from the station position for case 1 and within an interval between −2.4 and +4.8 km for case 2 (see method outline in previous section). From the ramp model, the estimated "midramp" is located within an interval between −2.4 and −4.2 km for case 1 and within an interval between −2.4 and +5.7 km for case 2. For station LKR, the RFs from both sides generate the deeper Moho
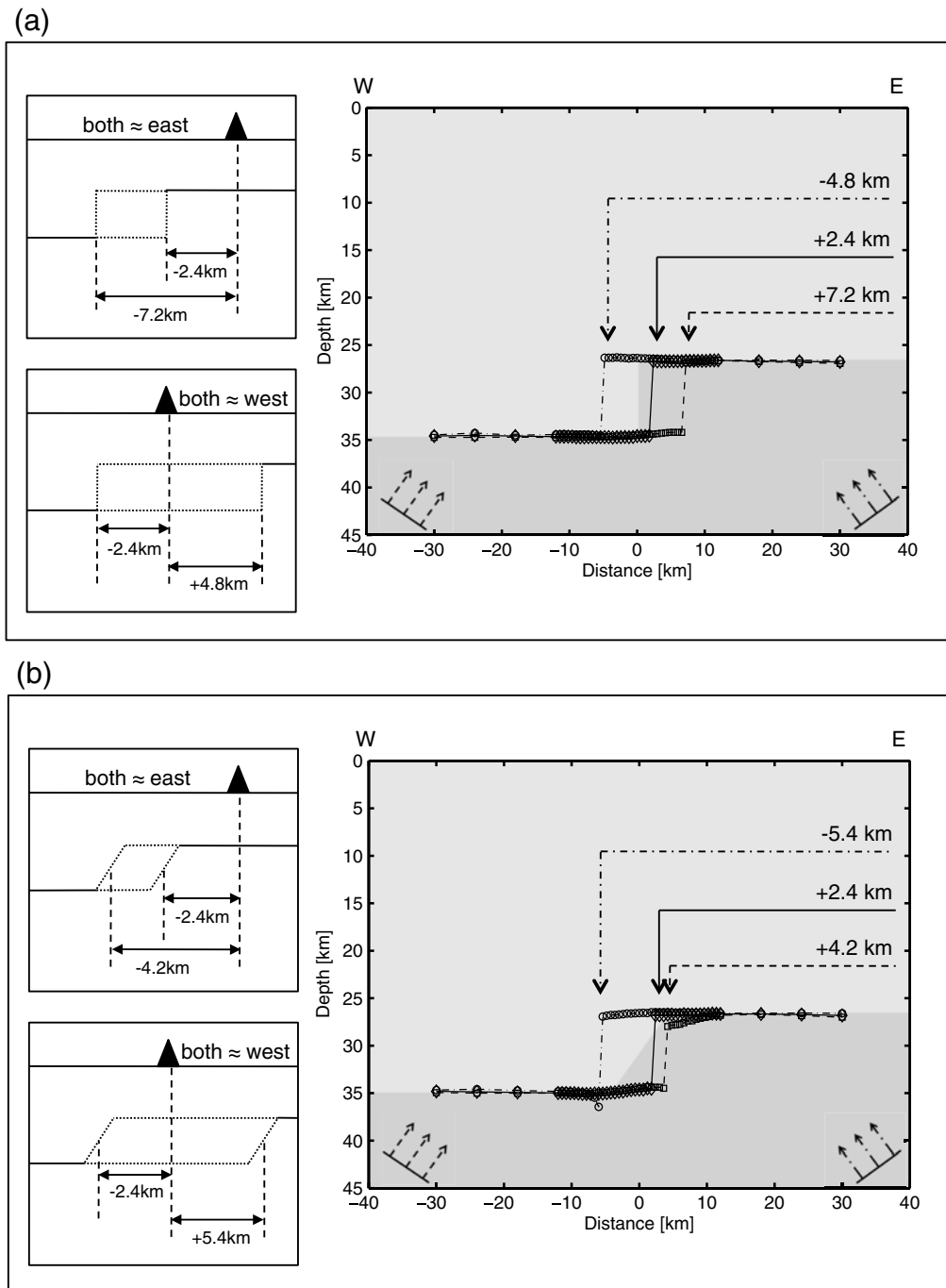
Figure 12. Lateral location ranges of an 8 km Moho offset from single-station RF analysis (noise free, (a) step model, (b) ramp model). See Ⓔ Figures S11 and S12 for the location ranges for the models with added noise.

depth, so the midramp is between −2.4 and +5.4 km from station LKR. Thus, the offset is located between −2.4 and +5.4 km in the direction from the southern boundary of the Kura basin to the Caspian Sea relative to station LKR (see Fig. 13). Ⓔ Figures S9 and S10 show how P_S arrival times control the estimated Moho depths for station LKR, in which synthetic RFs are stacked from the five events from the east and six events from the west. We also estimate the ranges for step and ramp offset models with added noise, shown in

Ⓔ Figures S11 and S12, respectively. For station LKR, the slant-staking method still produces a reasonable estimate of the Moho offset in the presence of realistic levels of noise in the RFs.

In the case in which several stations are available in a linear array on one side of a Moho offset, Ⓔ Figures S9 and S10 suggest additional clues on the location of the offset directly from the RFs. For example, in the case of LKR, a linear array on top of the shallow Moho side (east) would

Figure 13. The estimated location range of the Moho discontinuity below station LKR from our study (white dashed lines). The circled white symbol is the location of LKR. (Base map from Google Earth; see Data and Resources.)

record an abrupt ∼1 s decrease of the P-P_S delay from ∼6 to ∼9 km laterally from a step and from ∼3 to ∼6 km from a ramp for sources from the west. Likewise, multiple stations above the deep Moho side (west) would capture an abrupt ∼1 s decrease in P-P_S time ∼2 to ∼4 km laterally from an offset for sources from the east. Thus, the characteristics of RFs from a one-sided array contain important clues to the location of a potential Moho offset.

Finally, we show that the method still applies to more gradual (∼35° dip) Moho ramps, with ranges of the location of the ramp midpoint between −2.4 and +5.4 km for a 25–30 km offset ramp and between −3.6 and +6.6 km for a 30–35 km offset ramp (see Ⓔ Figs. S13 and S14). However, the pattern of the estimated depths for more gradual (35° and less) Moho ramps (27–35 km depth range) starts to diverge from the more abrupt Moho offsets (∼45° and steeper), causing the location method to fail (see Ⓔ Fig. S15). This result does not depend on the incidence angles of the RFs.

Conclusions

RFs have been proven to be a useful tool for estimating average crustal parameters in various geological settings around the world with the assumption of a 1D structure. Here, we have used a slant-stacking method combined with a 2D FD technique to examine the expected signature of radial 0–2 Hz P-wave RFs above a Moho discontinuity. RFs above the Moho discontinuity are characterized by a split P_S arrival with the different arrival timing representing the two

different thicknesses of the crust in the model. This pattern of the RFs generally persists in the vicinity of a ramp-like (∼45° or steeper) change of Moho depth, rather than a step, and appears robust in the presence of realistic noise.

We applied the slant-stacking technique by Zhu and Kanamori (2000) to estimate the optimal crustal parameters from the RFs computed near a Moho step or steep ramp. Even though this technique is based on forward modeling in a 1D crustal model, we still obtain estimates of abrupt changes in Moho depth. Although these estimated depth changes are slightly offset from the actual location of the step or the midpoint of the ramp, they provide the basis for a method to estimate the range of possible positions of the Moho discontinuity based on RFs from a single or a few stations. This method is applied to analyze observed RFs from station LKR in Azerbaijan, located on the western border of the Caspian Sea, on the boundary between the Talysh Mountains and the Kura basin. Our 2D model, with an ∼8 km step from a shallower Moho to the east and deeper to the west, generates synthetics in general agreement with the observed RFs for events incident from both east and west. To obtain more accurate estimates of the Moho depth variation below LKR, we suggest adding at least two nearby stations, one to the east and one to the west (currently not available).

Finally, our modeling study also suggests that the ZK2000 slant-stacking method can be a useful tool to detect lateral topography on the Moho, especially when seismic data are obtained from closely spaced stations along a linear array (with a relative distance of ∼10 km or less) incident from opposite directions along the array. We recommend that, as more RFs with high SNR ratios become available, future studies focus on further validating the indicators of the Moho offsets obtained in our study.

Data and Resources

The seismic data used to generate the receiver functions (RFs) at station LKR were provided by the Republican Seismic Survey Centre of Azerbaijan National Academy of Sciences. Figure 1 was created using Generic Mapping Tools, with topographic data from Becker *et al.* (2009) and station locations from the Euro-Med Bulletin (http://www.emsc-csem.org/Bulletin/, last accessed December 2015). Figure 13 was obtained via Google Earth, with the location of station LKR as 38°46'18.29" N and 48°59'11.34" E (Google Earth, 9 April 2013, https://www.google.com/earth/, last accessed September 2015).

Acknowledgments

References

Becker, J. J., D. T. Sandwell, W. H. F. Smith, J. Braud, B. Binder, J. Depner, D. Fabre, J. Factor, S. Ingalls, S.-H. Kim, *et al.* (2009). Global bathymetry and elevation data at 30 arc seconds resolution: SRTM30_PLUS, *Mar. Geodes.* **32,** no. 4, 355–371.

Bostock, M. G., R. D. Hyndman, S. Rondenay, and S. M. Peacock (2002). An inverted continental Moho and serpentinization of the forearc mantle, *Nature* **417,** 536–538.

Brunet, M. F., M. V. Korotaev, A. V. Ershov, and A. M. Nikishin (2003). The South Caspian basin: A review of its evolution from subsidence modeling, *Sediment. Geol.* **156,** nos. 1/4, 119–148.

Cerjan, C., D. Kosloff, R. Kosloff, and M. Reshef (1985). A nonreflecting boundary condition for discrete acoustic and elastic wave equations, *Geophysics* **50,** 705–708.

Fuchs, K., and G. Müller (1971). Computation of synthetic seismograms with the reflectivity method and comparison with observations, *Geophys. J. Roy. Astron. Soc.* **23,** 417–433.

Gök, R., R. J. Mellors, E. Sandvol, M. Pasyanos, T. Hauk, R. Takedatsu, G. Yetirmishli, U. Teoman, N. Turkelli, T. Godoladze, *et al.* (2011). Lithospheric velocity structure of the Anatolian plateau-Caucasus-Caspian regions, *J. Geophys. Res.* **116,** no. B05303, doi: 10.1029/2009JB000837.

Gottschaemmer, E., and K. B. Olsen (2001). Accuracy of the explicit planar free-surface boundary condition implemented in a fourth-order staggered-grid velocity-stress finite-difference scheme, *Bull. Seismol. Soc. Am.* **91,** 617–623.

Jacobsen, B. H., and L. Svenningsen (2008). Enhanced uniqueness and linearity of receiver function inversion, *Bull. Seismol. Soc. Am.* **98,** 1756–1767.

Kadinsky-Cade, K., M. Barazangi, J. Oliver, and B. Isacks (1981). Lateral variations of high-frequency seismic wave propagations at regional distances across the Turkish and Iranian plateaus, *J. Geophys. Res.* **86,** 9377–9396.

Knapp, C. C., J. H. Knapp, and J. A. Connor (2004). Crustal-scale structure of the South Caspian basin revealed by deep seismic reflection profiling, *Mar. Petrol. Geol.* **21,** 1073–1081.

Kosarev, G., R. Kind, S. V. Sobolev, X. Yuan, W. Hanka, and S. Oreshin (1999). Seismic evidence for a detached Indian lithospheric mantle beneath Tibet, *Science* **283,** no. 5406, 1306–1309.

Levander, A. R. (1988). A fourth-order accurate finite-difference scheme for the computation of elastic waves, *J. Geophys.* **53,** 1425–1436.

Ligorria, J. P., and C. J. Ammon (1999). Iterative deconvolution and receiver-function estimation, *Bull. Seismol. Soc. Am.* **89,** 1395–1400.

Mangino, S., and K. Priestley (1998). The crustal structure of the southern Caspian region, *Geophys. J. Int.* **133,** 630–648.

Sengör, A. M. C. (1990). A new model for the late Palaeozoic-Mesozoic tectonic evolution of Iran and implications for Oman, in *The Geology and Tectonics of the Oman Region*, A. H. F. Robertson, M. P. Searle, and A. C. Ries (Editors), *Geol. Soc. Spec. Publ.*, Vol. 49, 797–831, doi: 10.1144/GSL.SP.1992.049.01.49.

Yan, Z., and R. W. Clayton (2007). A notch structure on the Moho beneath the eastern San Gabriel Mountains, *Earth Planet. Sci. Lett.* **260,** 570–581.

Zhu, L., and H. Kanamori (2000). Moho depth variation in southern California from teleseismic receiver functions, *J. Geophys. Res.* **105,** 2969–2980.

Department of Geological Sciences
San Diego State University
MC-1020, 5500 Campanile Drive
San Diego, California 92182
kbolsen@mail.sdsu.edu